MSDE

PAPER

View Article Online
View Journal | View Issue

Check for updates

Cite this: *Mol. Syst. Des. Eng.*, 2025, 10, 662

Harnessing peptide–cellulose interactions to tailor the performance of self-assembled, injectable hydrogels†

Jessica A. Thomas, [a] Alex H. Balzer, [bc] Subhash Kalidindi [bc] and LaShanda T. J. Korley *[ab]

Received 26th January 2025,
Accepted 20th May 2025

DOI: 10.1039/d5me00009b

rsc.li/molecular-engineering

Taking inspiration from natural systems, such as spider silk and mollusk nacre, that employ hierarchical assembly to attain robust material performance, we leveraged matrix–filler interactions within reinforced polymer–peptide hybrids to create self-assembled hydrogels with enhanced properties. Specifically, cellulose nanocrystals (CNCs) were incorporated into peptide–polyurea (PPU) hybrid matrices to tailor key hydrogel features through matrix–filler interactions. Herein, we examined the impact of peptide repeat length and CNC loading on hydrogelation, morphology, mechanics, and thermal behavior of PPU/CNC composite hydrogels. The addition of CNCs into PPU hydrogels resulted in increased gel stiffness; however, the extent of reinforcement of the nanocomposite gels upon nanofiller inclusion also was driven by PPU architecture. Temperature-promoted stiffening transitions observed in nanocomposite PPU hydrogels were dictated by peptide segment length. Analysis of the peptide secondary structure confirmed shifts in the conformation of peptidic domains (α-helices or β-sheets) upon CNC loading. Finally, PPU/CNC hydrogels were probed for their injectability characteristics, demonstrating that nanofiller–matrix interactions were shown to aid rapid network reformation (~10 s) upon cessation of high shear forces. Overall, this research showcases the potential of modulating matrix–filler interactions within PPU/CNC hydrogels through strategic system design, enabling the tuning of functional hydrogel characteristics for diverse applications.

Design, System, Application

Nature achieves robust, dynamic materials by utilizing molecular building blocks and composite structures that result in hierarchical assembly. Inspired by high-performance natural materials such as spider silk and nacre, we present a nanocomposite design strategy to tailor the properties of non-covalent hydrogels. Our design employs cellulose nanocrystals (CNCs) as nanofillers in a peptide–polyurea (PPU) hybrid matrix to probe the impact of high aspect ratio, hydrogen-bonding motifs on network performance. We demonstrated that the degree of nanofiller incorporation, in addition to peptide segment length, drives hydrogel morphology, mechanical performance, thermal behavior, and self-healing ability. This approach connects key properties that influence the applicability of hydrogels, such as stiffness and mechanical recovery, to system design choices. This work will provide an enhanced understanding of polymer–peptide hybrid/nanofiller structure–property relationships and will aid the development of biomaterials utilized in injectable therapeutics and matrices for drug stabilization.

Introduction

Hydrated polymer networks (*i.e.*, hydrogels) are highly versatile soft materials with significant potential in various applications, including tissue engineering scaffolds and injectable therapeutics. To develop these advanced hydrogel systems, control over key material properties is vital to achieve a desired functionality.[1] For example, the stiffness and viscoelasticity of tissue matrices are known to significantly impact the differentiation of cells into specific cell types.[2–4] Designing biomaterials that can be tuned to display a wide range of mechanical properties is, therefore, a major need in this space.[5] In addition to hydrogels with controlled mechanics, non-covalent or self-assembled hydrogel materials often are desired for their ability to self-heal after damage (*e.g.*, shear), that may be applied during injection processes.[6–9] Additionally, thermally stable, self-assembled hydrogel matrices engineered to disassemble upon dilution

[a] *Materials Science and Engineering, University of Delaware, Newark, DE 19716, USA. E-mail: lkorley@udel.edu*
[b] *Chemical and Biomolecular Engineering, University of Delaware, Newark, DE 19716, USA*
[c] *Center for Plastics Innovation (CPI), University of Delaware, Newark, Delaware 19716, USA*

† Electronic supplementary information (ESI) available. See DOI: https://doi.org/10.1039/d5me00009b

Open Access Article. Published on 02 juni 2025. Downloaded on 01-06-2026 19:18:05.
This article is licensed under a Creative Commons Attribution-NonCommercial 3.0 Unported Licence.

This journal is © The Royal Society of Chemistry and IChemE 2025

Open Access Article. Published on 02 juni 2025. Downloaded on 01-06-2026 19:18:05.
This article is licensed under a Creative Commons Attribution-NonCommercial 3.0 Unported Licence.

are of great interest to overcome cold chains required for drug immobilization during transport, which are currently impractical for the distribution of therapeutics due to the high associated costs and infrastructure requirements.[10,11] However, non-covalent hydrogels that meet the requirements for dynamic systems are plagued by weak mechanical properties and poor performance over multiple deformation cycles.[12] Thus, it is challenging to merge the needs for dynamic, yet robust mechanical behavior in hydrogel design.

One route towards enhanced mechanical properties of hydrogels is through the use of nanofillers. The resulting multiphase material system displays superior properties (*e.g.*, stiffness) relative to the neat polymer.[13–15] This materials design strategy also occurs in natural systems, for example, the impressive strength of mollusk nacre is derived from the composite of aragonite in a protein matrix, resulting in highly ordered, lamellar structures.[16] In polymer nanocomposites, matrix–filler interactions dictate the reinforcement of the system. Nanofillers that exhibit high aspect ratios and abundant surface chemistries, such as cellulose nanocrystals (CNCs), are a particularly attractive option for modulating hydrogel properties through dynamic interactions.[17,18] For instance, previous work incorporating CNCs into poly(ethylene glycol) (PEG) and poly(oligoethylene glycol methacrylate) (POEGMA) networks resulted in significant mechanical reinforcement due to hydrogen bonding between the polymer backbone and carboxyl groups on the CNCs.[19,20] Additionally, CNCs overcome biocompatibility and scalability challenges associated with other fillers (*e.g.*, carbon nanotubes), making CNCs ideal fillers for biomaterials applications.[21,22]

When considering hydrogel matrix materials, peptide-based hydrogels have been shown to be advantageous materials, often exhibiting biocompatibility and dynamic self-assembly of polypeptide motifs.[23–27] Controlling physical interactions, such as hydrogen bonding, of peptide matrices through nanofiller inclusion can impact peptide assembly and drive changes in mechanical properties.[28,29] CNCs recently have shown great promise as nanofiller materials for peptidic matrices, where the incorporation of CNCs has resulted in superior performance of the nanocomposites *via* dynamic interactions between the CNCs and matrix.[30] For example, Zhang *et al.* demonstrated that incorporating CNCs into collagen-based hydrogels resulted in improved shear-thinning behavior and aided the mechanical stability of mesenchymal stem cells during injection processes.[30] Nanocellulose–protein interactions also have been shown to drive toughening of silk-like polymers by promoting increased ordering of the peptide domains.[31] However, utilizing sequence-specific polypeptides as matrix materials has significant practical limitations, including scalability and synthetic methods, such as solid-phase peptide synthesis, that inherently limit molecular weights.[32–34]

One approach to address these drawbacks is through the use of polymer–peptide hybrids as the hydrogel matrix. Polymer–peptide hybrids provide the scalability and ease of fabrication of conventional synthetic polymers and maintain the structural and functional characteristics of peptides.[35,36] These hybrid materials have been studied across many applications, including hydrogel building blocks and drug delivery platforms, in which their hierarchical assembly and material performance are largely dictated by peptide secondary structure (*i.e.*, α-helices and β-sheets).[37–41] However, examples of CNC-containing, polymer–peptide hybrids used as hydrogel nanocomposite matrices are limited, with most nanocomposites utilizing graphene oxide or carbon nanotubes as nanofillers.[28,42] Silk-inspired, peptide–polyurea hybrids (PPUs) are particularly advantageous as a matrix polymer, as tailored peptide and synthetic polymer blocks interactions allow for tunable properties with high molecular weights that can drive hierarchical assembly. For instance, Jang *et al.* recently demonstrated that matrix–filler (PPU–CNC) interactions significantly influenced the peptidic ordering, hydrogen-bonding arrangement, microphase-separated morphology, and mechanical properties of polydimethylsiloxane (PDMS)-based PPU/CNC solid-state films.[43] In previous work, our group showed that PEG-based PPUs can be utilized as a platform for self-assembled, injectable hydrogels.[44] There remains opportunities to expand the utility of PPU hydrogels through nanofiller incorporation, specifically, increasing the range of hydrogel mechanical properties, controlling thermal behavior, and improving strain-recovery dynamics; however, the influence of CNCs on PPU hydrogel properties remains relatively unexplored. In this work, we systematically evaluate the impact of CNC incorporation on PPU hydrogel mechanics, morphology, and thermal stability. Two multiblock copolymers containing PEG and poly(ε-carbobenzyloxy-L-lysine) (PZLY) segments were synthesized with controlled peptide repeat lengths (5 or 40) within the chain. Morphological and mechanical characterizations were performed to elucidate the impact of non-covalent interactions with CNC nanofiller at various loadings. Incorporation of CNC nanofiller resulted in significant reinforcement of hydrogel moduli with up to 1825% and 239% increases in storage moduli for repeat lengths of 5 and 40, respectively. Interestingly, the shear recovery of PPU hydrogels during injection simulation experiments was maintained, and in some cases improved, along with this increase in gel stiffness. Overall, we present PPU/CNC nanocomposites as a versatile platform for robust, injectable, hydrogel nanocomposites with tunable properties.

Experimental

Materials

Tetrahydrofuran (THF, Optima™ LC/MS grade), anhydrous *N*,*N*-dimethylacetamide (DMAc), deuterated chloroform, and diethyl ether were purchased from Fisher Scientific. THF was dried using a solvent purification system (Vacuum Atmosphere Company). All other solvents were used as

Open Access Article. Published on 02 juni 2025. Downloaded on 01-06-2026 19:18:05.
This article is licensed under a Creative Commons Attribution-NonCommercial 3.0 Unported Licence.

received. ε-Carbobenzyloxy-L-lysine (ZLY), triphosgene, (≥99%), dibutyltin dilaurate (DBTDL), and 1,6-hexamethylene diisocyanate (HDI) (≥99%, stored in glovebox) were purchased from Sigma-Aldrich and used as received. ε-Carbobenzyloxy-L-lysine *N*-carboxyanhydride (ZLY-NCA) was prepared according to previously established literature procedures.[45] α,ω-Bis(amine)poly(ethylene glycol) (PEG diamine, 3400 g mol^{-1}) was purchased from SINO-PEG (Xiamen, P.R. China) and dried under vacuum at room temperature for 16 h and then at 60 °C for 4 h before use in synthetic procedures. All glassware was oven dried prior to use. TEMPO-cellulose nanocrystals (CNCs) suspended in water with a carboxyl group content of 2.6 $mmol^{-1}$ were obtained from Cellulose Lab (Canada). These CNCs are approximately 4 nm in width and 150 nm in length. These CNCs were precipitated *via* solvent exchange with acetone and dried under vacuum prior to use.

PPU synthesis

As reported previously, non-chain extended PZLY PPUs were synthesized by employing PZLY-*b*-PEG-*b*-PZLY triblocks as the soft segment.[46] Two triblocks with controlled peptide repeat lengths (5, 40) were prepared *via* ring-opening polymerization of ZLY-NCA using PEG diamine as the initiator. The resulting PZLY-*b*-PEG-*b*-PZLY copolymers were used as the soft segment in non-chain extended PPUs by reacting with PEG diamine and hexamethylene diisocyanate. Samples are designated by the nomenclature Z*N*-*X*, where *N* denotes the peptide repeat length and *X* represents the peptide weight percent in the polyurea. Polymerizations were carried out in a glovebox under a nitrogen atmosphere. The final weight PZLY percentage in the polyurea was determined using eqn (S1) (ESI†). As an example, the synthesis of Z5-10 is described. Hexamethylene diisocyanate (HDI) (1 mol) was added to a solution of 25 vol% DMAc in THF (10 mL) in a 50 mL single-neck, round bottom flask equipped with a magnetic stirrer. Z5-*b*-PEG-*b*-Z5 (0.20 g, 0.15 mol) and PEG diamine (0.64 g, 0.85 mol) were dissolved in 10 mL of 25 vol% DMAc in THF in a glass vial, along with 5 drops of DBTDL as a catalyst. This Z5-*b*-PEG-*b*-Z5 soft segment solution was added dropwise to the round bottom flask, and then capped with a Vigreux condenser. The reaction was allowed to proceed at 60 °C for 18 h. The resulting polymer then was precipitated into diethyl ether, collected by vacuum filtration, and dried under vacuum at 22 °C, yielding a white, rubbery solid.

NMR

The chemical structures of ZLY-NCA and the resulting triblock copolymers were verified through ^{1}H nuclear magnetic resonance spectroscopy (^{1}H-NMR). Samples were dissolved in $CDCl_3$, and the spectra were recorded at room temperature using a Bruker AVIII 400 MHz spectrometer. Spectra and peak assignments are provided in Fig. S1–S3 of the ESI.† The data were analyzed using MNOVA software.

GPC

The average molecular weights and molecular weight distributions of the PPUs were measured using a TOSOH EcoSEC Elite GPC system equipped with a refractive index detector and TSKgel columns (three SuperH and one SuperAW5000 column in series). 0.08 mL of sample at a concentration of 0.5 mg mL^{-1} was injected and eluted at 0.4 mL min^{-1} with 0.5 wt% LiBr in DMAc as the mobile phase. Molecular weight distributions were generated using the calibration curve constructed for six poly(methyl methacrylate) standards (Agilent) in the range of 0.885 to 2210 kg mol^{-1}.

Nanocomposite hydrogel fabrication

To form the PPU/CNC nanocomposite hydrogels, CNCs first were suspended at the desired concentrations (5 or 10 wt% of the final hydrogel mass) in 0.01 M PBS buffer. Dry CNCs were weighed into glass vials, to which appropriate amounts of PBS buffer were added *via* volumetric pipette. The CNC/buffer solutions then were suspended utilizing a bath sonicator until fully dispersed (~30 min), as indicated by a visually homogeneous, clear solution. PPUs were then weighed and added to the CNC/buffer solution to fabricate nanocomposite gels at 10 wt% polymer and mixed using an orbital shaker at 22 °C until visually homogeneous. Control PPU hydrogels with no CNC content also were fabricated at 10 wt% polymer in 0.01 M PBS buffer. The control and PPU/CNC nanocomposite hydrogels successfully passed the gel inversion test, meaning they did not flow under gravity.

Cryogenic Transmission Electron Microscopy (Cryo-TEM)

PPU/CNC hydrogels were applied to 400 mesh copper lacey carbon grids, manually blotted with filter paper, and plunge frozen into liquid ethane using a Thermo Scientific Mark IV Vitrobot. Due to the high viscosity of the hydrogels, a reproducible method to achieve a thin layer of hydrogel was developed. Filter paper was affixed to two glass microscope slides, and one slide was used to support the back of the grid, whereas the second slide was used to manually smear the hydrogel across the grid. The frozen grids were imaged on a Thermo Scientific Talos L120C operating at 120 kV using a Gatan Elsa cryo-holder. Standard low dose techniques were used to acquire images with a Thermo Scientific Ceta-M camera at a total dose of 15–20 electrons per $Å^2$ to prevent sample damage. Fiber diameters from TEM were measured in ImageJ software, where the measurement tool was calibrated to the known distance of the scale bar for each individual image.

Scanning Electron Microscopy (SEM)

SEM micrographs were obtained using a JSM 7400F-SEM (JEOL, Tokyo, Japan) at an accelerating voltage of 5 kV. PPU/CNC hydrogel samples were frozen with liquid nitrogen,

 This journal is © The Royal Society of Chemistry and IChemE 2025

Open Access Article. Published on 02 juni 2025. Downloaded on 01-06-2026 19:18:05.
This article is licensed under a Creative Commons Attribution-NonCommercial 3.0 Unported Licence.

lyophilized for 72 h, and sputter-coated with gold–palladium (Au–Pd) alloy for 60 s using a Denton Desk IV sputter coater (Denton Vacuum LLC, Moorestown, NJ, USA) prior to imaging. Pore diameters were measured using ImageJ software, where the measurement tool was calibrated to the known distance of the scale bar for each individual image. We acknowledge that freezing and lyophilization of hydrogels can potentially introduce artifactual pore-like structures through the removal of solvent; however, porous structures observed in these samples are consistent with previous study of PPU hydrogels.[44]

Rheology

Rheological analysis of the PPU/CNC nanocomposite gels was performed as reported previously.[44] Briefly, the rheological properties of the fabricated gels were assessed using a stress-controlled rheometer (DHR-3, TA Instruments) with a parallel plate setup (20 mm diameter) and Peltier heating. Samples were loaded with a plastic spatula, placing the desired amount on the bottom plate pre-equilibrated at the testing temperature. Samples then were compressed to fill the gap between the plates (1 mm) and trimmed. To prevent water evaporation during measurement, the exposed edges of samples were coated with a thin layer of silicone oil. The axial force and temperature were allowed to stabilize before starting the experiment.

First, mechanical characterization was conducted on all gel systems at 37 °C. Samples were pre-sheared for 300 s at a strain amplitude of 0.1% and a frequency of 1 rad s^{-1} to remove any stress from loading. A frequency sweep then was performed between 0.1 rad s^{-1} and 100 rad s^{-1} at a 0.5% strain amplitude, chosen beforehand to prevent gel breakup before characterization. A strain amplitude sweep was subsequently conducted to confirm that the chosen strain amplitude was within the linear viscoelastic regime (LVR). This amplitude sweep was carried out at 1 rad s^{-1}, with strain amplitudes ranging from 0.01% to 1000%.

Next, step-strain experiments were carried out on control and nanocomposite PPU/CNC hydrogels to assess their behavior under injection conditions. To measure microstructural changes during shear without incurring potential adverse effects of slip or edge fracture between parallel plates, oscillatory shear was implemented. This experiment was performed in six segments; first, a 30 s step at 1 rad s^{-1} and 200% strain amplitude was applied, immediately followed by a segment at 1 rad s^{-1} and 0.1% strain. Moduli were observed, and the next high strain step was initiated once both moduli remained constant. These two consecutive experimental conditions were then repeated to observe cyclic recovery behavior. For the final segment, deformation occurred for 60 s at the same conditions used in previous steps, followed by the same procedure to monitor network re-formation. A 'fast sampling' procedure was used in all stages such that the stress and strain waveforms were continuously acquired.

Finally, thermorheological properties were assessed by varying the temperature during oscillation. The samples were cooled from 37 °C to 5 °C, then heated from 5 °C to 80 °C, and cooled again from 80 °C to 5 °C, at a rate of 2 °C min^{-1}. During this thermal cycling, the hydrogels were subjected to 0.1% strain and a frequency of 1 rad s^{-1}.

Photothermal Infrared Spectroscopy (PTIR)

PTIR was performed on all PPU/CNC hydrogel samples utilizing a mIRage® IR microscope (Photothermal Spectroscopy Corp.). Hydrogel samples were lightly spread on a glass slide and loaded onto the microscope stage. Imaging was performed with probe power and IR power set at 5% and 22%, respectively. The detector gain was set at 10×. Three scans were performed at each sampling spot. Gaussian deconvolution of the amide I region was performed using Origin software.

Differential Scanning Calorimetry (DSC)

Differential scanning calorimetry (DSC) was performed using a Discovery DSC instrument (TA Instruments). Approximately 25 mg of each hydrogel was hermetically sealed in an aluminum crucible. The temperature was controlled using the instrument's Modulated DSC (MDSC) technique, in which a sinusoidal oscillation (1 °C amplitude, 120 s period) was overlaid on a linear heating or cooling ramp (2 °C min^{-1}). The sample temperature was controlled between −90 °C and 80 °C, with 2 min isotherms after each ramp, under nitrogen flow. The instrument software (TRIOS; TA Instruments) calculates the reversing, non-reversing, and total heat flow from the MDSC scan. The first and last 2 min oscillations of the MDSC scan were excluded from heat flow calculations due to software requirements; thus, the heat flow data is only reported between approximately −86 °C and 76 °C, though the sample still reached the intended temperature endpoints, as confirmed by temperature data. All DSC plots are oriented as endotherm up.

Results & discussion

This work builds upon previous strategies to formulate non-covalent PPU hydrogels with tunable properties, aiming to use hydrogen-bonding nanofillers as an additional handle to expand key property ranges of PPU gels. CNCs are ideal nanofillers to incorporate into this hydrogel platform, due to their surface functionality, biocompatibility, and ability to modulate peptidic ordering and mechanics in other PPU matrices.[43,47,48] Herein, the impact of CNC nanofiller inclusion on PPU network morphology, rheological behavior, thermal properties, and secondary structure composition is examined. PZLY-*b*-PEG-*b*-PZLY triblock copolymers were employed as the soft block in linear, non-chain extended PPUs to achieve rapid gelation of the hydrated PPU matrix (Fig. 1A). The PZLY repeat length (5 or 40) was controlled, as peptide segment length is expected to modulate the

Open Access Article. Published on 02 juni 2025. Downloaded on 01-06-2026 19:18:05.
This article is licensed under a Creative Commons Attribution-NonCommercial 3.0 Unported Licence.

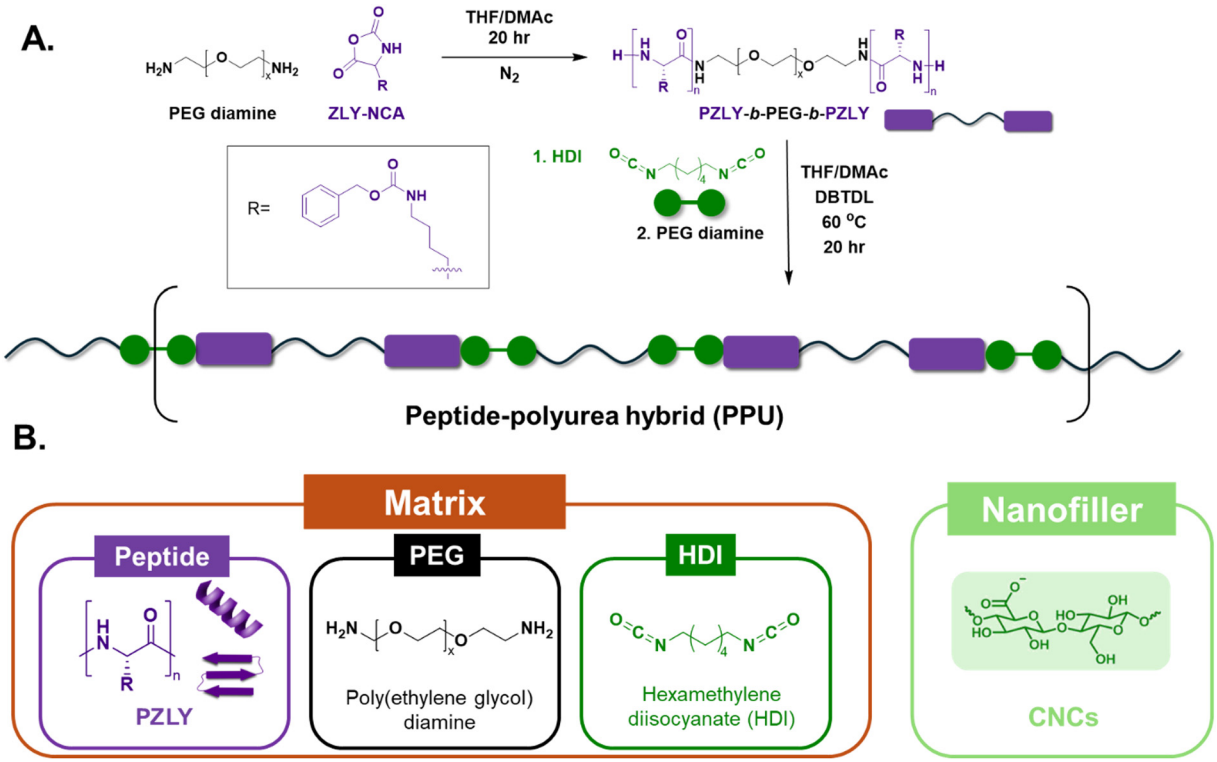

Fig. 1 A. Synthetic scheme of PPU hydrogel matrix. B. Components (matrix and nanofiller) of PPU/cellulose nanocrystal (PPU/CNC) nanocomposite hydrogels.

secondary structure distribution, moduli, and critical strain of PPU/CNC nanocomposites.[44] The PZLY content was maintained at 10 wt% across all PPU samples to specifically address the role of peptide chain length, as changes in peptide composition can also affect PPU properties.[49,50] Fig. S4 and Table S1† detail the molecular weight distributions of both PPUs, which are of sufficient molecular weight (109 kg mol^{-1} and 110 kg mol^{-1}) to result in intra-chain interactions required to attain silk-like mechanics.[51]

Fabrication, nanostructure, and morphology of nanocomposite hydrogels

To examine the impact of CNC content on hydrogel properties, PPU/CNC nanocomposites were fabricated at varying nanofiller concentrations (0, 5, and 10 wt% of total hydrogel mass). CNCs were dispersed in 0.01 M PBS buffer at the desired concentrations and sonicated until a clear, free flowing solution was obtained. An appropriate mass of PPU polymer then was added to the CNC/buffer solution to maintain the polymer : water mass ratio (1 : 9), allowing for consistent hydration and a controlled comparison of how varying CNC content affects hydrogel properties. The PPU/CNC solutions then were shaken at room temperature, resulting in visually homogeneous hydrogels. Sonication of the resulting PPU/CNC hydrogels was avoided to prevent heating and/or potential degradation to the nanocomposite hydrogels prior to further experiments. The following nomenclature was applied to neat PPUs and PPU/CNC nanocomposites (Fig. 1B): Z*N*-*X*/CN*C*Y, in which *Z* denotes PPUs made from PZLY-*b*-PEG-*b*-PZLY, *N* represents the PZLY block length, *X* indicates the peptide content, and *Y* specifies the CNC weight fraction in the PPUs. Z*N*-*X*/CNC0 refers to the control PPU hydrogels.

The gelation behavior of PPU/CNC nanocomposites was observed with a vial inversion test (Fig. 2A), confirming that Z5-10/CNC and Z40-10/CNC nanocomposites form self-supporting hydrogels. In this work, two microscopy techniques were chosen in order to observe different features of the PPU/CNC hydrogels; SEM was implemented to observe morphological features of the hydrogel surface, whereas TEM was applied to analyze internal nanostructures. To observe any potential impacts of CNC incorporation on PPU hydrogel nanostructure, cryo-TEM was performed. Previous work with PPU hydrogel self-assembly revealed that dense fiber networks drive gelation in all samples.[44] In this current study, fiber networks also were observed in the TEM micrographs (Fig. 2B and S13†) of Z5-10/CNC5, Z5-10/CNC10, Z40-10/CNC5, and Z40-10/CNC10 nanocomposites; fiber diameters across all samples were approximately 8 ± 1 nm, indicating association of multiple PPU chains, which agrees well with previous analysis of PPU hydrogel nanostructures.[44] Similar fibrous networks have been seen in self-assembled peptide amphiphiles, which have been observed to pack into physical hydrogels, and lysine homopolymers, where α-helical nanostructures were achieved in high molecular

 This journal is © The Royal Society of Chemistry and IChemE 2025

Open Access Article. Published on 02 juni 2025. Downloaded on 01-06-2026 19:18:05.
This article is licensed under a Creative Commons Attribution-NonCommercial 3.0 Unported Licence.

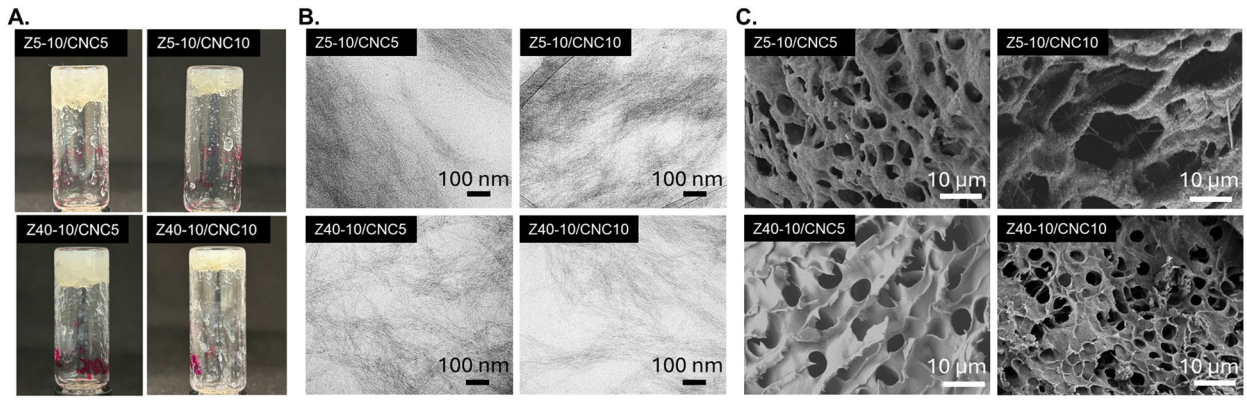

Fig. 2 A. Vial inversion experiments of PPU/CNC nanocomposite hydrogels confirming gelation at 5 and 10 wt% CNC loading. B. Cryo-TEM images of Z5-10/CNC5, Z5-10/CNC10, Z40-10/CNC5, and Z40-10/CNC10 reveal fibrous structures in all PPU/CNC nanocomposites. C. SEM images of Z5-10/CNC0, Z5-10/CNC10, Z40-10/CNC5, and Z40-10/CNC10 show continuous porous networks.

weight species.[52–54] Overall, the presence of fiber networks in cryo-TEM micrographs indicate that the CNCs do not significantly disrupt the PPU self-assembly, and suggest that favorable interactions exist between the nanofiller and PPU hydrogel matrix.

The inclusion of nanofillers in polymer hydrogels can have a significant impact on porosity, which is a key parameter for material performance in a variety of applications, such as therapeutic matrices or tissue engineering scaffolds.[55] CNCs often influence the pore structure of hydrogel materials as a result of increased hydrogen bonding between surface groups present on the CNCs and the polymer matrix.[56] To evaluate the morphology of PPU/CNC nanocomposites, SEM was performed (Fig. 2C and S12†). All PPU/CNC nanocomposites demonstrated continuous porous structures with smaller average pore sizes than observed in neat controls (30 ± 5 μm: Z5-10/CNC0; 19 ± 5 μm: Z40-10/CNC0), indicating that increased hydrogen bonding led to a reduction in the mesh size in for PPU nanocomposite networks. In the Z5-10/CNC series, the pore size was comparable across the nanocomposites: 5 ± 1.5 μm for the 5 wt% CNC PPU hydrogels and 7 ± 2 μm for the 10 wt% PPU hydrogels. Interestingly, incorporation of CNCs into the PPU hydrogel matrix resulted in more uniform, circular pores in the Z40-10 series as shown in Fig. 2C. In the Z40-10 series, as the CNC loading increased, the average pore size decreased from approximately 7 ± 1.5 μm to 3 ± 0.6 μm. These findings indicate that the CNCs significantly impacted the pore morphology of the Z40-10/CNC series, resulting from increased hydrogen bonding between the filler and matrix and agree with the DSC analysis of free *vs.* bound water in the Z40-10/CNC series in the thermal behavior section below.

Mechanical analysis of PPU/CNC nanocomposites

Evaluating the viscoelastic mechanics of hydrogel materials is vital, as characteristics including moduli and critical strain, impact their suitability for a variety of applications. For example, the modulus of a hydrogel matrix has significant impacts on cell growth and differentiation.[57] The storage moduli of PPU/CNC hydrogels taken at 6.28 rad s^{-1} (1 Hz) spanned from approximately 120 to 3300 Pa, a range comparable to various soft tissues, including those found in the extracellular matrix, liver, brain, and lungs.[58] Frequency sweeps for the Z5-10 and Z40-10 nanocomposite series at various CNC loadings (0, 5, and 10 wt%) are displayed in Fig. 3A and B. In all cases, the storage modulus exceeds the loss modulus ($G' > G''$), which is characteristic of a viscoelastic network.[26] As previously reported, the moduli of the Z40-10/CNC0 control exceeds that of the Z5-10/CNC0 control, attributed to longer α-helical peptide domains providing increased stability to network junctions.[44] In comparison to the Z5-10/CNC0 control (Fig. 3A), G' (1 rad s^{-1}) increased by 3.6× and 18.2× at CNC loadings of 5 and 10 wt%, respectively. In contrast, increases in G' in the Z40-10/CNC series were less pronounced, in which the storage moduli of the Z40-10 series (Fig. 3B) increased by 1.3× and 2.4× at CNC loadings of 5 and 10 wt%, respectively. This reduction in the extent of reinforcement in Z40-10/CNC10 compared to Z5-10/CNC10 is linked to the hydrogen-bonding arrangements of the CNCs within the PPU matrix and the resulting impact on peptide secondary structure, which will be addressed in the secondary structure analysis section below.

A summary of mechanical trends in PPU/CNC nanocomposite hydrogels is displayed in Fig. 3B. In addition to storage moduli, changes in the critical strain, defined as the strain at which the storage modulus decreased by 5 percent, also are highlighted in Fig. 3C and D, where values of storage moduli and critical strain of the samples shown in Fig. 3A and B are provided as a visual representation of trends in mechanical properties as a function of CNC inclusion. Full amplitude sweeps of all PPU/CNC nanocomposites are provided in Fig. S5.† In the Z5-10/CNC series, the critical strain first decreased sharply from 13% to 5.3% upon 5 wt% CNC loading, then to 3.2% at 10 wt% CNC loading. For the Z40-10/CNC series, however, the critical strain decreased only slightly from 3.3% in the Z40-10/CNC0

Open Access Article. Published on 02 juni 2025. Downloaded on 01-06-2026 19:18:05.
This article is licensed under a Creative Commons Attribution-NonCommercial 3.0 Unported Licence.

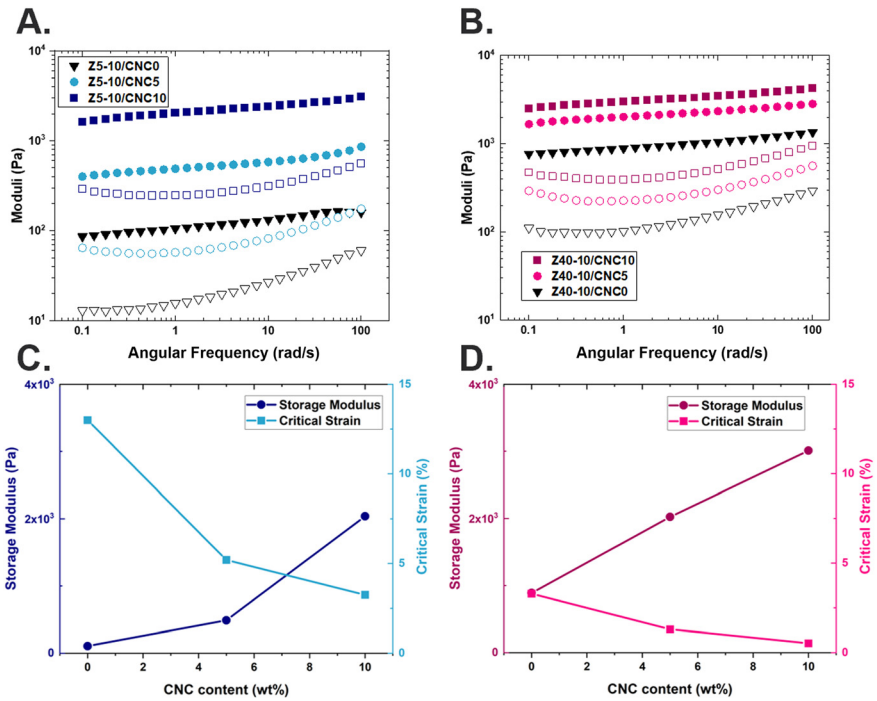

Fig. 3 A) Angular frequency sweeps of Z5-10/CNC series and B) Z40-10 CNC series at 37 °C; open symbols indicate the storage moduli (G'), and closed symbols indicate the loss moduli (G''). Summary of trends in G' at 1 rad s^{-1} and critical strain as a function of CNC loading for C) Z5-10/CNC series and D) Z40-10/CNC series.

control to 1.3% and 0.5% at the 5 wt% and 10 wt% CNC loadings, respectively. A lower critical strain is typically associated with facile injection of hydrogels, as less force is needed to result in dissociation of the viscoelastic network.[59] The combination of increasing stiffness and decreasing critical strain upon CNC loading suggests that reinforcement of the network moduli will not hinder potential injection applications.[19,60–62] This decrease in critical strain with increased CNC loading across both sample sets confirms that CNC–peptide interactions dictate the strain at which gel breakup occurs, thus providing a convenient handle for adjusting injectable hydrogel parameters. Overall, CNC incorporation significantly impacts the mechanics of PPU hydrogels, increasing gel stiffness as function of nanofiller concentration. However, the extent of reinforcement (*i.e.*, increase in G', G'') and impact on critical strain from CNCs also is shown to be dependent on PPU architecture.

Impact of CNCs on thermal and mechanical behavior of hydrogel nanocomposites

Peptide-based hydrogel systems often undergo structural shifts in response to temperature changes.[63] It is important to understand thermally driven changes in mechanical properties, as they can impact the performance of hydrogels in applications in which stability during incubation or storage conditions for therapeutics is needed. To observe the rheological stability of PPU/CNC hydrogels, temperature ramps, shown in Fig. 4A and D, were performed. In both the Z5-10/CNC and Z40-10/CNC series, PPU hydrogels displayed a reduction in storage moduli upon heating (closed symbols) from 20 °C to 80 °C, which has previously been attributed to slight melting and reorganization of α-helical peptidic structures.[44] Upon cooling (open symbols), hysteretic behavior was observed as the modulus is increased, which is more significant in the Z5-10/CNC hydrogels. Incorporation of CNCs into the PPU matrix has a significant impact on the hysteresis pathway of the nanocomposite hydrogels, which can be more clearly seen in the Z5-10 series (Fig. 4A). Interestingly, the presence of CNCs in the Z5-10 matrix results in an increase in storage moduli during the cooling cycle, the opposite behavior of the control. Importantly, this stiffening behavior is not observed in the non-CNC containing control samples, indicating that CNC incorporation, not water loss, is driving these thermomechanical changes. This change in thermorheological performance is likely a result of hydrogen-bonding CNCs influencing the structural rearrangement of the peptide segments. Previous studies on the effects on structural reorganization of CNCs in polymer melts suggest that, in some cases, the CNCs undergo phase separation to a more entropically favored state as a result of thermal annealing.[64,65] However, there is limited understanding of the impacts of temperature on polymer–peptide hybrid/CNC nanocomposite materials, particularly in the hydrated state. To probe the stiffening behavior and hysteresis observed in PPU/CNC hydrogels, thermal analysis *via* temperature-modulated DSC was performed. Z5-10/CNC0 did not exhibit any melting endotherm between 20 °C and 80 °C, suggesting that its

 This journal is © The Royal Society of Chemistry and IChemE 2025

Open Access Article. Published on 02 juni 2025. Downloaded on 01-06-2026 19:18:05.
This article is licensed under a Creative Commons Attribution-NonCommercial 3.0 Unported Licence.

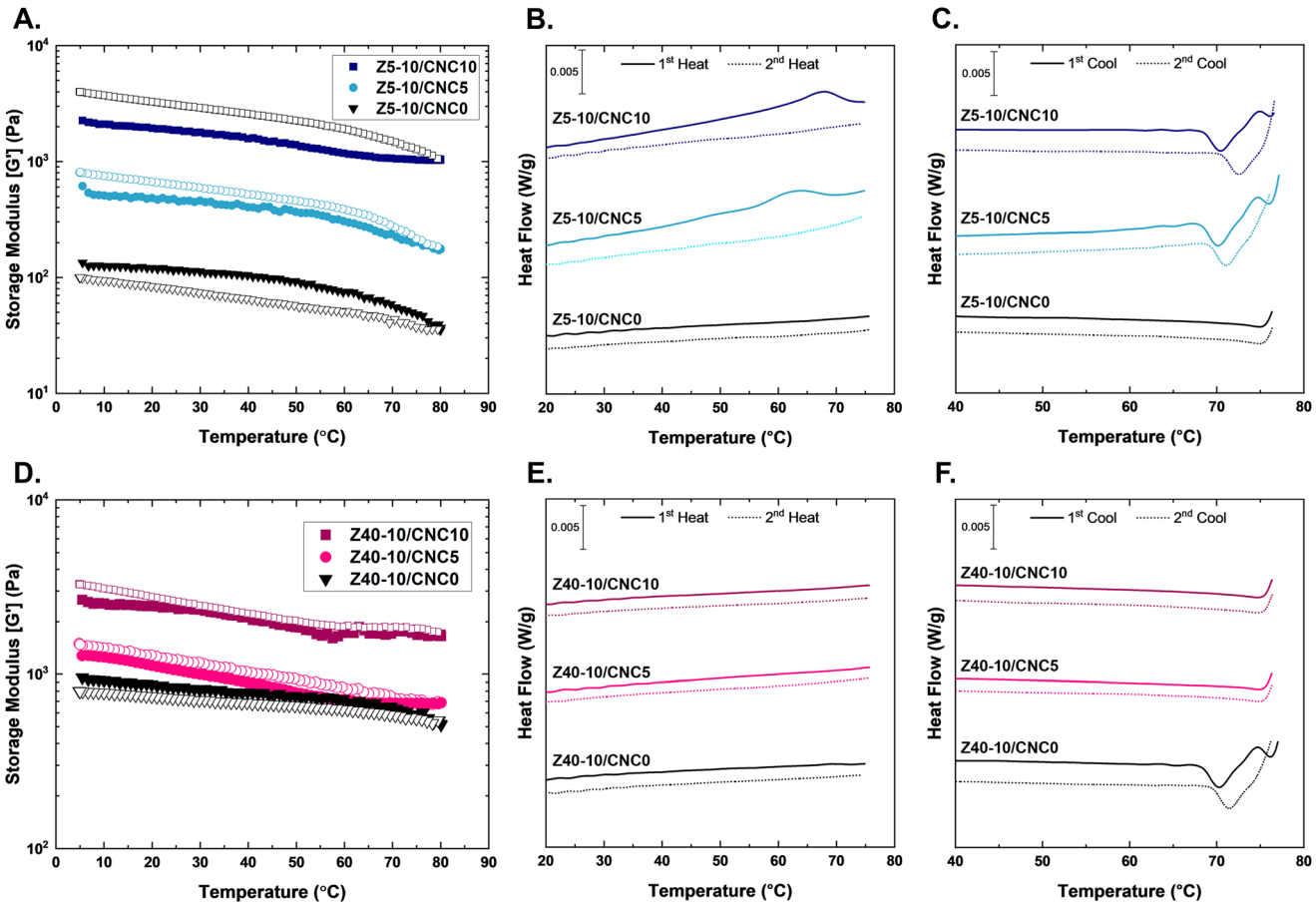

Fig. 4 A. Storage moduli (G') during temperature ramps (10–80 °C) of Z5-10/CNC series; closed symbols indicate the heating cycle, while open symbols indicate the cooling cycle. Upon CNC incorporation, thermal hysteresis switches from softening to stiffening upon cooling. B. DSC heating scans of Z5-10/CNC hydrogel series. C. DSC cooling scans of Z5–10/CNC series. D. Storage moduli during temperature ramps (10–80 °C) of Z40-10/CNC series. E. DSC heating scans of Z40-10/CNC hydrogel series. F. DSC cooling scans of Z40-10/CNC series.

softening was due to peptide motif reorganization, as has been previously observed (Fig. 4B).[44] However, when CNCs were incorporated into the Z5-10 matrix (Z5-10/CNC5, Z5-10/CNC10), melting endotherms appeared at temperatures similar to the thermal transition ranges seen in the PPU/CNC hydrogel rheology (Fig. 4B). These high-temperature transitions are attributed to the melting of PEG–peptide hybrid crystals/assemblies, as their crystallization temperature during cooling occurred above the equilibrium melting point of PEG (69 °C).[66] This crystallization drives the stiffening behavior of the Z5-10/CNC gels during the cooling ramps. To evaluate the reversibility of the melting and crystallization processes, the samples were thermally cycled twice. No apparent melting was observed during the second heating, except for a slight slope increase in Z5-10/CNC5 around 72 °C. Interestingly, the crystallization exotherms occurred at higher temperatures than during the first cooling, indicating that incomplete melting had occurred by 80 °C, and higher temperatures are likely needed for full thermal reversibility; however, rapid water loss *via* evaporation/boiling is expected above 80 °C, and thus was not attempted. In contrast to Z5-10/CNC0, Z40-10/CNC0 exhibited a crystallization exotherm during cooling, attributed to a similar microstructural transformation as Z5-10/CNC gels (*i.e.*, peptide hybrid crystals/assemblies). However, the longer peptide length in Z40-10 would allow for the formation of larger structures, which were not detectable *via* DSC in the tested temperature range. DSC traces of Z40-10/CNC (Z40-10/CNC5, Z40-10/CNC10) hydrogels did not display melting or crystallization events, correlating with their reduced hysteresis and stiffening compared to Z5-10/CNC (Z5-10/CNC5, Z5-10/CNC10) gels. Longer peptide repeat lengths are expected to result in more stable α-helical domains, resulting in less thermal rearrangement of PPU chains, which agrees with rheological studies in Fig. 4D and prior investigations.[49,67,68] Despite these findings, some softening and subsequent stiffening still occurred, suggesting that 80 °C is too low to fully melt any microstructure, though it may anneal any crystalline structure, increasing crystal volume and order.

To examine any thermally driven changes in hydrogel porosity and morphology, the distribution of free water, freezable-bound water, and non-freezing bound water was calculated. CNC incorporation increased the fraction of free and freezable-bound water, likely due to enhanced hydrogen bonding between peptide sequences and CNCs rather than

Open Access Article. Published on 02 juni 2025. Downloaded on 01-06-2026 19:18:05.
This article is licensed under a Creative Commons Attribution-NonCommercial 3.0 Unported Licence.

between peptide moieties and water. This trend was more evident in Z40-10 hydrogels (Fig. S10†) and agrees with SEM analysis of reduced pore sizes with increased CNC loading, as well as PTIR trends discussed further below. After thermal cycling, the hydrogels exhibited similar levels of free and bound water, suggesting that the pore morphology remained mostly unaltered during the process. Lastly, each hydrogel had a glass transition temperature (T_g) at approximately −67 °C (Table S2†), attributed to a plasticized (*via* water) PEG–peptide amorphous phase. The consistency of the T_gs among all samples was expected because the peptide-content was maintained at 10 wt%. Additionally, the presence of CNCs did not affect the T_g, which assuming the T_g reported is the mobile-amorphous fraction, suggests a phase-separated PPU/CNC system.[69] Z40-10 displayed a slightly lower T_g (−70 °C) than Z5-10, yet differences in free and bound water content makes definitive conclusions about the relationship between peptide length and T_g challenging. The decrease in ΔC_p at T_g (Table S2†) was linked to further interactions between PPU and the rigid CNCs, similar to effects seen in polyol-clay nanocomposites, and crystal annealing due to incomplete melting, given the 80 °C limit.[70] The similar T_gs across all samples suggest comparable chain stiffness in the PPU hybrids, and the overall reduction in ΔC_p at T_g after thermal cycling confirms that the stiffening behavior largely results from crystalline phase formation and possibly some peptide conformational changes.[71,72] Thus, it is clear that thermally driven mechanical changes in PPU/CNC nanocomposite hydrogels are a result of different microstructures and bulk (pore) morphologies dictated by both CNC loading and peptide segment length, emphasizing the role of PPU architecture on hydrogel performance.

Secondary structure analysis & impact of CNC incorporation on peptidic ordering in PPU hydrogels

Characterization of hydrogen-bonding arrangement and secondary structure conformation in PPU/CNC nanocomposite hydrogels is necessary to understand the impact of matrix–filler interactions on key aspects of material performance, such as mechanical and thermal properties. Photothermal infrared spectroscopy (PTIR) can be employed to assess secondary structure (α-helix and β-sheet) shifts and hydrogen-bonding interactions present in PPU/CNC nanocomposite hydrogels, as this non-contact technique facilitates improved resolution for samples that cannot be analyzed as thin films.[73,74] In Fig. 5, the amide I region (1625–1700 cm^{-1}) of the Z5-10 and Z40-10 nanocomposite series were examined to confirm changes in secondary structure in each sample set as CNC loading was increased. A peak between 1650 and 1670 cm^{-1} is associated with α-helical structures, whereas a signal between 1625 and 1645 cm^{-1} is indicative of β-sheet formation.[46,75] To quantify the relative amounts of secondary structure conformation present in each sample, Gaussian deconvolution was performed (Fig. S7†), with results shown in Table 1. Additionally, the region at 1600–1625 cm^{-1}, attributed to urea group ordering, is observed.[76]

Neat PPU hydrogels (Z5-10/CNC0, Z40-10/CNC0) all contain a mixture of α-helix and β-sheet structures, although the α-helix is the dominant conformation in all cases. This conformation preference is consistent with previous analysis of PPU hydrogels, where the primary secondary structure, as measured by circular dichroism spectroscopy, was found to be α-helical.[44] In the Z5-10/CNC (Z5-10/CNC5, Z5-10/CNC10) nanocomposite series, the peak intensity in the 1625–1645 cm^{-1} region decreased with each CNC loading (5, 10 wt%), resulting in a sequential increase in the α-helix fraction (Fig. 5A, Table 1). This peak shift suggests that, for the Z5-10 series, CNC incorporation interrupts the intermolecular hydrogen bonding of β-sheet structures, driving the peptide segments to increasingly adopt intramolecular α-helical conformations as more CNCs are added into the hydrogel and short peptide segments are driven further apart from one another. In contrast, the Z40-10/CNC nanocomposite series (Z40-10/CNC5, Z40-10/CNC10) displayed a different trend in secondary structure shift than expected. Z40-10/CNC5 still showed an increase in α-helix fraction compared to the neat control; however, Z40-10/CNC10 displayed a slight increase (~3%) in β-sheet fraction. This behavior suggests that PPUs with longer peptide segments undergo some

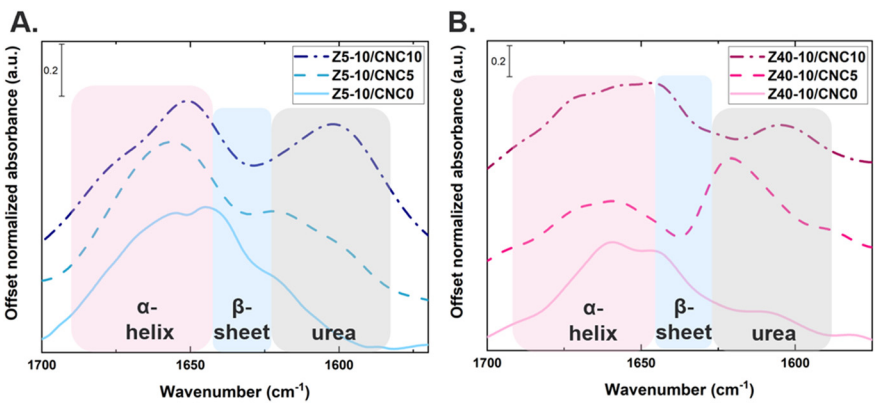

Fig. 5 PTIR investigation of the amide I region (1700–1600 cm^{-1}) of A. Z5-10/CNC series and B. Z40-10/CNC series as a function of CNC weight fraction.

This journal is © The Royal Society of Chemistry and IChemE 2025

Open Access Article. Published on 02 juni 2025. Downloaded on 01-06-2026 19:18:05.
This article is licensed under a Creative Commons Attribution-NonCommercial 3.0 Unported Licence.

Table 1 Relative quantity of peptide secondary structure as a function of PZLY repeat length and CNC loading

Sample	CNC loading (wt%)	α-helix (%)	β-sheet (%)
Z5-10	0	75	25
	5	84	16
	10	90	10
Z40-10	0	61	39
	5	72	28
	10	69	31

α-helix disruption at high CNC loadings, indicating increased peptide-CNC interactions which is likely a result of spatial packing of the PPU, and has been previously observed in PPU/CNC nanocomposites with peptide segment lengths greater than 5.[43] In comparison, in the Z5-10/CNC series (Z5-10/CNC5, Z5-10/CNC10), short peptide segments are more likely to be isolated, resulting in a continuous increase of intramolecular α-helix formation. Another important observation is that, across all PPU/CNC nanocomposite series, the peak at ~1600–1625 cm^{-1} becomes more intense and occasionally shifts to higher wavenumbers upon CNC loading. This signal is typically associated with urea group ordering in polyurea/PEG blends, indicating that the carboxylic acid groups present on the CNC surface are inducing enhanced hydrogen bonding with the PPU backbone.[77] Thus, the difference in CNC impact on secondary structure shifts of PPUs with different peptide segment lengths can be attributed to hydrogen bonding between the matrix and filler. Overall, the PTIR results suggest that both CNC content and choice of peptide architecture can be harnessed to tune secondary structure conformations of PPU hydrogels.

Impact of CNC inclusion on injection behavior

For a material to be considered appropriate for injection-based applications, it must possess a reversible structure—meaning the network should transition to a liquid-like state during injection and then re-form afterward, as clinical injections of such biomaterials are expected to involve significant shear forces. It has been reported that the inclusion of CNCs in peptidic hydrogel matrices can facilitate improved self-healing properties under injection conditions as a result of dynamic intermolecular interactions between polypeptide motifs and the CNCs.[30] A demonstration of PPU/CNC injectability is shown in Fig. 6A, where a 2 mL volume of Z40-10/CNC5 could be easily expelled through a syringe with human force. Videos demonstrating injectability of PPU/CNC hydrogels are provided in the ESI.† To confirm the self-healing behavior of the PPU/CNC nanocomposite gel structure, rheological step-strain experiments were performed to simulate injection conditions. Fig. 6B demonstrates the mechanical behavior of PPU/CNC nanocomposite gels throughout the step-strain oscillation cycles, using Z40-10/CNC5 as a representative example. Hydrogels were deformed beyond the critical strain for 30 s for 2 cycles, and 60 s for an additional third cycle, where it can be observed that $G'' > G'$ occurs, signifying a transition to liquid-like behavior. In all PPU/CNC nanocomposite hydrogels, rapid recovery from shear was observed over multiple cycles (Fig. S6†). The third and final recovery cycles for all hydrogels in the Z40-10/CNC series are compared in Fig. 6C. Notably, the Z40-10/CNC0 control required a longer period (>100 s) to recover its original moduli compared to the Z5-10/CNC0 control as a result of stiffer network mechanics. The addition of CNCs into the Z40-10 hydrogel resulted in a notable decrease in the time required for the hydrogels to fully regain their initial moduli (>100 s to ~30 s). This decrease in network recovery time is attributed to the strong hydrogen bonding interactions between the PPU matrix and CNCs, preventing excessive disruption of network junctions and resulting in rapid reformation of the hydrogel structure. Overall, the incorporation of CNCs allows for simultaneous tuning of hydrogel mechanics along with improved injectability properties, highlighting the utility of the PPU/CNC platform.

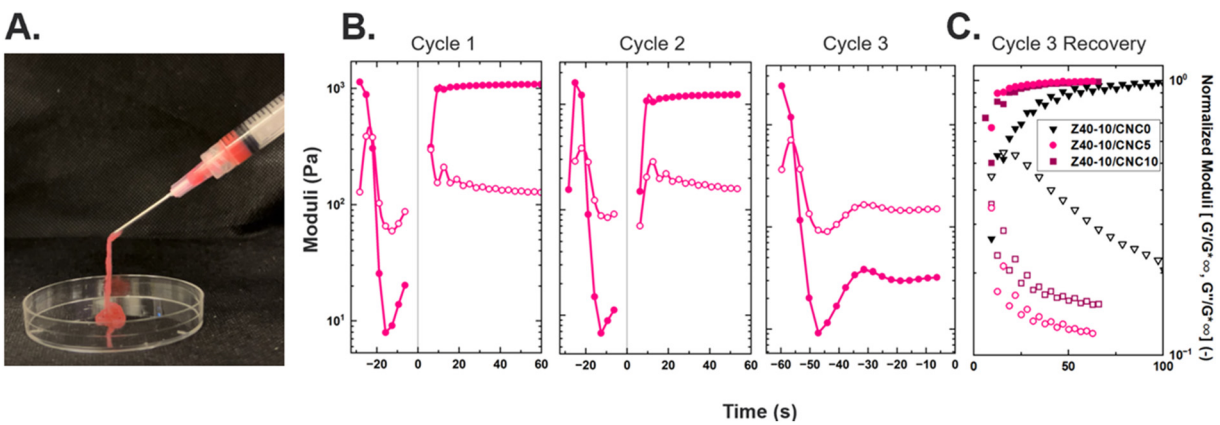

Fig. 6 A. Injection demonstration of Z40-10/CNC5 hydrogel through an 18-gauge needle; a small amount of red food dye was added to the hydrogel as a visual aid. B. Step-strain recovery cycles for Z40-10/CNC5. C. Third recovery cycle of Z40-10/CNC0, Z40-10/CNC5 and Z40-10/CNC10. Open symbols indicate the loss moduli, while closed symbols indicate storage moduli.

Open Access Article. Published on 02 juni 2025. Downloaded on 01-06-2026 19:18:05.
This article is licensed under a Creative Commons Attribution-NonCommercial 3.0 Unported Licence.

Conclusions

In this work, we designed and fabricated PPU/CNC hydrogels to utilize peptide–cellulose interactions as an additional handle to tune mechanical properties and thermal behavior in non-covalently assembled gels. It was shown that extent of CNC incorporation, in addition to peptide architecture, impacts morphology, peptide conformation, mechanics, and thermal response in PPU/CNC nanocomposites. Increasing CNC loading resulted in corresponding increases in gel moduli, but the magnitude of reinforcement also was dependent on peptide repeat length, highlighting the importance of system design choices. The influence of CNC–peptide interactions impacting hydrogel performance also was observed during thermal analysis, where crystallization phenomena resulted in mechanical stiffening upon thermal annealing in the Z5-10/CNC5 and Z5-10/CNC10 hydrogels, likely a result of increased mobility of the shorter α-helical domains. These key differences in the influence of CNC incorporation on the properties of PPU hydrogels were further elucidated by secondary structure analysis of PPU/CNC nanocomposites. At lower peptide repeat lengths (5), incorporation of CNCs at 5 and 10 wt% resulted in an increase in the α-helix fraction of the nanocomposite hydrogels. However, at higher peptide repeat lengths (40), disruption of α-helix conformations to β-sheets is observed at 10 wt% CNC incorporation, indicating that both CNC concentration and peptide repeat length dictate self-assembly behavior of the peptide domains. An advantage of including CNCs as hydrogen-bonding nanofillers in PPU hydrogels was demonstrated in step-strain experiments, where Z40-10/CNC nanocomposite gels displayed a significantly faster recovery time from strain-induced network disruption than the non-CNC containing control. The rapid self-healing behavior of these nanocomposite hydrogels highlights their suitability for high-shear applications, such as in injectable biomaterials. Overall, PPU/CNC nanocomposites show great utility as a design strategy to achieve self-assembled hydrogels with robust properties, with potential applications in therapeutic storage and delivery. Future work in developing this platform will explore avenues to achieve nanofiller alignment in PPU hydrogels to achieve increased hierarchical assembly and functionality in these materials.

Data availability

All data supporting this article are available in the main text or have been included as part of the ESI.†

Conflicts of interest

There are no conflicts to declare.

Acknowledgements

This work was supported by the National Science Foundation (NSF) PIRE: Bio-inspired Materials and Systems under grant number OISE 1844463. The authors acknowledge the use of facilities and instrumentation supported by NSF through the University of Delaware Materials Research Science and Engineering Center DMR-2011824. Differential scanning calorimetry characterization activities were supported by the Center for Plastics Innovation, an Energy Frontier Research Center funded by the U.S. Department of Energy, Office of Science, Basic Energy Sciences, under award DE-SC0021166. Cryo-TEM access was supported by grants from the NIH-NIGMS (P20 GM103446), the NIGMS (P20 GM139760) and the State of Delaware. Microscopy equipment was acquired with the Unidel Foundation. We thank Shannon Modla in the DBI Bio-Imaging Center for assistance with obtaining cryo-TEM images. Access to SEM was provided by the Keck Microscopy Center at the University of Delaware. PTIR access was provided by the University of Delaware Advanced Materials Characterization Laboratory.

References

1 H. Cao, L. Duan, Y. Zhang, J. Cao and K. Zhang, *Signal Transduction Targeted Ther.*, 2021, **6**, 1–31.
2 A. Elosegui-Artola, A. Gupta, A. J. Najibi, B. R. Seo, R. Garry, C. M. Tringides, I. de Lázaro, M. Darnell, W. Gu, Q. Zhou, D. A. Weitz, L. Mahadevan and D. J. Mooney, *Nat. Mater.*, 2023, **22**, 117–127.
3 C. J. O'Conor, N. Case and F. Guilak, *Stem Cell Res. Ther.*, 2013, **4**, 1–13.
4 M. B. Keogh, F. J. O'Brien and J. S. Daly, *Acta Biomater.*, 2010, **6**, 4305–4313.
5 K. Zhang, Q. Feng, Z. Fang, L. Gu and L. Bian, *Chem. Rev.*, 2021, **121**, 11149–11193.
6 S. Correa, A. K. Grosskopf, H. L. Hernandez, D. Chan, A. C. Yu, L. M. Stapleton and E. A. Appel, *Chem. Rev.*, 2020, **121**, 11385–11457.
7 C. Yan, A. Altunbas, T. Yucel, R. P. Nagarkar, P. Schneider and D. J. Pochan, *Soft Matter*, 2010, **6**, 5143–5156.
8 J. H. Lee, *Biomater. Res.*, 2018, **22**, 1–14.
9 Y. Li, H. Y. Yang and D. S. Lee, *Biomacromolecules*, 2022, **23**, 609–618.
10 R. P. Welch, H. Lee, M. A. Luzuriaga, O. R. Brohlin and J. J. Gassensmith, *Bioconjugate Chem.*, 2018, **29**, 2867–2883.
11 C. M. Meis, E. E. Salzman, C. L. Maikawa, A. A. A. Smith, J. L. Mann, A. K. Grosskopf and E. A. Appel, *ACS Biomater. Sci. Eng.*, 2021, **7**, 4221–4229.
12 L. E. Beckett, J. T. Lewis, T. K. Tonge and L. T. J. Korley, *ACS Biomater. Sci. Eng.*, 2020, **6**, 5453–5473.
13 X. Li, W. Xu, Y. Xin, J. Yuan, Y. Ji, S. Chu and J. Liu, *Polymers*, 2021, **13**, 1–17.
14 S. Fu, Z. Sun, P. Huang, Y. Li and N. Hu, *Nano Mater. Sci.*, 2019, **1**, 2–30.
15 P. Thoniyot, M. J. Tan, A. A. Karim, D. J. Young and X. J. Loh, *Adv. Sci.*, 2015, **2**, 1–13.
16 R. A. Metzler, J. S. Evans, C. E. Killian, D. Zhou, T. H. Churchill, N. P. Appathurai and S. N. Coppersmith, *J. Am. Chem. Soc.*, 2010, 6329–6334.

This journal is © The Royal Society of Chemistry and IChemE 2025

Open Access Article. Published on 02 juni 2025. Downloaded on 01-06-2026 19:18:05.
This article is licensed under a Creative Commons Attribution-NonCommercial 3.0 Unported Licence.

17 K. J. De France, T. Hoare and E. D. Cranston, *Chem. Mater.*, 2017, **29**, 4609–4631.
18 J. R. Capadona, K. Shanmuganathan, D. J. Tyler, S. J. Rowan and C. Weder, *Science*, 2008, **319**, 1370–1374.
19 J. Yang, C. R. Han, J. F. Duan, F. Xu and R. C. Sun, *ACS Appl. Mater. Interfaces*, 2013, **5**, 3199–3207.
20 K. J. De France, K. J. W. Chan, E. D. Cranston and T. Hoare, *Biomacromolecules*, 2016, **17**, 649–660.
21 E. Heister, E. W. Brunner, G. R. Dieckmann, I. Jurewicz and A. B. Dalton, *ACS Appl. Mater. Interfaces*, 2013, **5**, 1870–1891.
22 Y. Liu, Y. Zhao, B. Sun and C. Chen, *Acc. Chem. Res.*, 2013, **46**, 702–713.
23 C. B. Thompson and L. T. J. Korley, *Bioconjugate Chem.*, 2017, **28**, 1325–1339.
24 A. K. Nguyen, T. G. Molley, E. Kardia, S. Ganda, S. Chakraborty, S. L. Wong, J. Ruan, B. E. Yee, J. Mata, A. Vijayan, N. Kumar, R. D. Tilley, S. A. Waters and K. A. Kilian, *Nat. Commun.*, 2023, **14**, 6604.
25 A. Panitch, J. Chmielewski and C. M. R. Pe, *Macromol. Biosci.*, 2011, **11**, 1426–1431.
26 C. Yan and D. J. Pochan, *Chem. Soc. Rev.*, 2010, **39**, 3528–3540.
27 P. Katyal, M. Meleties and J. K. Montclare, *ACS Biomater. Sci. Eng.*, 2019, **5**, 4132–4147.
28 W. W. Lei, L. Y. Shi, H. Li, C. X. Li, Y. F. Diao, Y. L. Zhang and R. Ran, *RSC Adv.*, 2017, **7**, 1471–1479.
29 I. Leppänen, S. Arola, A. W. T. King, M. Unger, H. Stadler, G. S. Nissen, C. Zborowski, T. Virtanen, J. Salmela, H. Setälä, S. Lésage, M. Österberg and T. Tammelin, *Adv. Mater. Interfaces*, 2023, **10**, 2300162.
30 S. Zhang, D. Huang, H. Lin, Y. Xiao and X. Zhang, *Biomacromolecules*, 2020, **21**, 2400–2408.
31 P. Mohammadi, A. Sesilja Aranko, C. P. Landowski, O. Ikkala, K. Jaudzems, W. Wagermaier and M. B. Linder, *Sci. Adv.*, 2019, **5**, 1–11.
32 A. Miserez, J. Yu and P. Mohammadi, *Chem. Rev.*, 2023, **123**, 2049–2111.
33 N. C. Abascal and L. Regan, *Open Biol.*, 2018, **8**, 180113.
34 S. S. Hou, N. S. Fan, Y. C. Tseng and J. S. Jan, *Macromolecules*, 2018, **51**, 8054–8063.
35 C. Chen, D. Y. W. Ng and T. Weil, *Prog. Polym. Sci.*, 2020, **105**, 101241.
36 I. W. Hamley, *Biomacromolecules*, 2014, **15**, 1543–1559.
37 F. Zhang, C. Hu, Q. Kong, R. Luo and Y. Wang, *ACS Appl. Mater. Interfaces*, 2019, 37147–37155.
38 K. Tomoyuki, A. Shioi and N. Higashi, *Biomacromolecules*, 2022, **23**, 2941–2950.
39 E. Radvar and H. S. Azevedo, *Macromol. Biosci.*, 2018, **1800221**, 1–16.
40 N. I. Halaszynski, J. G. Saven, D. J. Pochan and C. J. Kloxin, *Bioconjugate Chem.*, 2023, **34**, 2001–2006.
41 A. Sarkar, C. Edson, D. Tian, T. D. Fink, K. Cianciotti, R. A. Gross, C. Bae and R. H. Zha, *Biomacromolecules*, 2021, **22**, 95–105.
42 V. Wulf and G. Bisker, *Nano Lett.*, 2022, **22**, 9205–9214.
43 D. Jang, L. E. Beckett, J. Keum and L. T. J. Korley, *J. Mater. Chem. B*, 2023, **11**, 5594–5606.
44 J. A. Thomas, Z. R. Hinton and L. T. J. Korley, *Soft Matter*, 2023, **41**, 7912–7922.
45 S. N. Smith and S. J. Connon, *Eur. J. Org. Chem.*, 2024, **27**, 1–7.
46 L. E. Matolyak, J. K. Keum, K. M. Van De Voorde and L. T. J. Korley, *Org. Biomol. Chem.*, 2017, **15**, 7607–7617.
47 S. Imlimthan, A. Correia, P. Figueiredo, K. Lintinen, V. Balasubramanian, A. J. Airaksinen, M. A. Kostiainen, H. A. Santos and M. Sarparanta, *J. Biomed. Mater. Res., Part A*, 2020, **108**, 770–783.
48 R. J. Moon, A. Martini, J. Nairn, J. Simonsen and J. Youngblood, *Chem. Soc. Rev.*, 2011, **40**, 3941–3994.
49 L. E. Matolyak, C. B. Thompson, B. Li, J. K. Keum, J. E. Cowen, R. S. Tomazin and L. S. T. J. Korley, *Biomacromolecules*, 2018, **19**, 3445–3455.
50 D. Jang, C. B. Thompson, S. Chatterjee and L. T. J. Korley, *Mol. Syst. Des. Eng.*, 2021, **6**, 1003–1015.
51 J. C. Johnson and L. T. J. Korley, *Soft Matter*, 2012, **8**, 11431–11442.
52 L. Hsu, G. L. Cvetanovich and S. I. Stupp, *J. Am. Chem. Soc.*, 2008, **130**, 3892–3899.
53 J. D. Hartgerink, E. Beniash and S. I. Stupp, *Proc. Natl. Acad. Sci. U. S. A.*, 2002, **99**, 5133–5138.
54 K. Cie, *Biochimie*, 2017, **137**, 106–114.
55 F. J. O'Brien, *Mater. Today*, 2011, **14**, 88–95.
56 A. Trubetskaya, J. Leppiniemi, S. Lipponen, S. Lombardo, W. Thielemans, T. Maloney, T. Pääkkönen, K. K. Kesari, J. Ruokolainen, V. P. Hytönen and E. Kontturi, *Mater. Adv.*, 2023, **5**, 570–583.
57 C. F. Guimarães, L. Gasperini, A. P. Marques and R. L. Reis, *Nat. Rev. Mater.*, 2020, **5**, 351–370.
58 O. Chaudhuri, J. Cooper-white, P. A. Janmey, D. J. Mooney and V. B. Shenoy, *Nature*, 2020, **584**, 535–546.
59 T. E. Robinson, E. A. B. Hughes, A. Bose, E. A. Cornish, J. Y. Teo, N. M. Eisenstein, L. M. Grover and S. C. Cox, *Adv. Healthcare Mater.*, 2020, **9**, 1901521.
60 E. Kushan and E. Senses, *ACS Appl. Bio Mater.*, 2021, **4**, 3507–3517.
61 D. J. Overstreet, D. Dutta, S. E. Stabenfeldt and B. L. Vernon, *J. Polym. Sci., Part B*, 2012, 881–903.
62 M. H. Chen, L. L. Wang, J. J. Chung, Y. H. Kim, P. Atluri and J. A. Burdick, *ACS Biomater. Sci. Eng.*, 2017, **3**, 3146–3160.
63 A. M. Jonker, D. W. P. M. Löwik and J. C. M. Van Hest, *Chem. Mater.*, 2012, **24**, 759–773.
64 P. K. Annamalai, K. L. Dagnon, S. Monemian, E. J. Foster, S. J. Rowan and C. Weder, *ACS Appl. Mater. Interfaces*, 2014, **6**, 967–976.
65 M. Mariano, N. El Kissi and A. Dufresne, *Langmuir*, 2016, **32**, 10093–10103.
66 B. Wunderlich, *Pure Appl. Chem.*, 1995, **67**, 1019–1026.
67 J. C. Johnson, N. D. Wanasekara and L. T. J. Korley, *J. Mater. Chem. B*, 2014, **2**, 2554–2561.
68 L. Matolyak, J. Keum and L. S. T. J. Korley, *Biomacromolecules*, 2016, **17**, 3931–3939.
69 H. Suzuki, J. Grebowicz and B. Wunderlich, *Br. Polym. J.*, 1984, **17**, 1984–1986.

Open Access Article. Published on 02 juni 2025. Downloaded on 01-06-2026 19:18:05.
This article is licensed under a Creative Commons Attribution-NonCommercial 3.0 Unported Licence.

70 H. Xia and M. Song, *Thermochim. Acta*, 2005, **429**, 1–5.
71 X. Hu, D. Kaplan and P. Cebe, *Thermochim. Acta*, 2007, **461**, 137–144.
72 X. Hu, D. Kaplan and P. Cebe, *Macromolecules*, 2016, 3939–3948.
73 M. Rahmati, S. Stötzel, T. El Khassawna, C. Mao, A. Ali, J. C. Vaughan, K. Iskhahova, D. C. Florian Wieland, A. G. Cantalapiedra, G. Perale, F. Betge, E. P. Dillon, S. P. Lyngstadaas and H. J. Haugen, *Mater. Today*, 2022, **52**, 63–79.
74 D. Ami, P. Mereghetti and A. Natalello, *Front. Mol. Biosci.*, 2022, **9**, 1–7.
75 M. Jackson and H. H. Mantsch, *Crit. Rev. Biochem. Mol. Biol.*, 1995, **30**, 95–120.
76 V. Timón, B. Maté, V. J. Herrero and I. Tanarro, *Phys. Chem. Chem. Phys.*, 2021, **23**, 22344–22351.
77 J. Mattia and P. Painter, *Macromolecules*, 2007, **40**, 1546–1554.

 This journal is © The Royal Society of Chemistry and IChemE 2025